CHEMISTRY OF MATERIALS

pubs.acs.org/cm Article

Multiresponse Shape-Memory Nanocomposite with a Reversible Cycle for Powerful Artificial Muscles

Chi Chen, Yangyuanchen Liu, Ximin He, Hua Li, Yujie Chen,* Ying Wei, Yusen Zhao, Yanfei Ma, Zhen Chen, Xu Zheng, and Hezhou Liu*

Cite This: *Chem. Mater.* 2021, 33, 987−997 Read Online

ACCESS | Metrics & More | Article Recommendations | Supporting Information

ABSTRACT: In the field of bionic soft robots and microrobots, artificial muscle materials have exhibited unique potential for cutting-edge applications. However, current mainstream thermal-responsive artificial muscles based on semicrystalline polymers (SCPs), despite their excellent physical properties, suffer from the limitation of environmental stimuli in practice, while their photodriven counterparts adopting liquid crystal elastomers (LCEs) lack ductility. Herein, a novel multifunctional programmable artificial muscle with a unique patch-sewing structure formed by $\pi-\pi$ stacking between azobenzene groups was designed, which combined the advantages of SCPs and LCEs. The nanocomposite demonstrated a unique combination between artificial muscle performance (46.5 times the energy density and 26.6 times the power density of human skeletal muscles) and programmability (274.84% strain and 100% shape-memory recovery rate within 1 s). Meanwhile, coupling the photoisomerization of azobenzene and the photothermal conversion of gold nanorods, the cycle of deformation triggered by ultraviolet light and restoring by infrared light could be accomplished rapidly within 30 s. A COMSOL Multiphysics model was established and the corresponding finite element analysis verified the photoactuation and captured the general principle of light initiation in elastomers. These demonstrate that the multifunctional programmable elastomer is promising for artificial muscle applications, especially for photoinduced actuation.

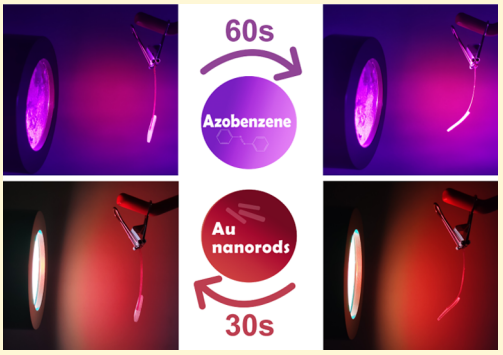

INTRODUCTION

Artificial muscles capable of generating considerable forces and motions are recognized as a promising solution to alleviating the tremendous pressure of renewable materials and robot design.[1] Over the past 20 years, various actuators based on artificial muscles have gained momentum in the fields of micro-aerial vehicles,[2] jack grippers,[3] bionic designs,[4] etc. Compared with traditional materials used in actuators, polymer-based materials have excellent properties such as exceptional formability, low cost, and high elasticity.[5] Through the elaborate design of configurations and conformations, the overall performances can be augmented with large deformation,[6] self-healing,[7] multiple stimulus responses,[8] etc. Among polymer-based materials, shape-memory polymers (SMPs) based on a shape-memory effect (SME) occupy an indispensable position in soft robots and artificial muscles.[9] This is due to the distinguished stimulus-response capability and programmability of shape-memory polymers, where the contraction and release of muscles correspond to the deformation and recovery of polymers, respectively. Among various SMPs, two-way and quasi-two-way materials with reversible cycling properties, such as semicrystalline polymers (SCPs)[10] and liquid crystal elastomers (LCEs), are undoubtedly more promising.[11] The long-chain skeleton providing unique ductility as well as plasticity and the response elements exhibiting a rapid phase transition as well as controlled orientation exactly meet the two benchmarks of SMPs (i.e., the mechanical and responsive properties).[12] In recent years, researchers have reported a large amount of work related to the stimulus-responsive actuators and a large proportion of them still employ thermal triggers. Nevertheless, whether it is pure thermal initiation[13] or electrothermal initiation,[14] the reliance of heating on physical contact prevents the thermal uniformity and lowers the reverse stimulation efficiency of the entire material on account of the specific heat capacity. Besides, the contact-induced actuation also makes it challenging to apply the material to remotely controllable or precisely controllable devices, such as untethered robots. To remedy these defects, light-driven SMPs have attracted extensive attention by introducing specific organic groups (azobenzene,[15] spiropyran,[16] etc.) or inorganic groups (graphene,[17] metal nano-

Received: October 27, 2020
Revised: January 8, 2021
Published: January 19, 2021

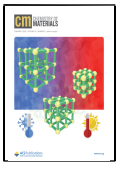

https://dx.doi.org/10.1021/acs.chemmater.0c04170
Chem. Mater. 2021, 33, 987−997

particles,[18] etc.) into the polymer matrix. These light-responsive molecules can undergo isomerization under specific light irradiation and reversibly transform between at least two chemical or aggregated structures. As a result, these isomerization reactions will change the ordered arrangement inside the molecular chain, which can be expressed in different colors and obvious deformation at a macroscale.[19] In contrast to thermally induced actuators, light-driven systems have the huge advantages of instantaneous control, environmental friendliness, and noncontact initiation.[20] Another notable challenge is to make the balance between the response performance and the physical properties, including strength, strain, ductility, and plasticity of SMPs. Although LCEs exhibit unparalleled response performance and large mechanical strength, their insufficient flexibility makes it difficult in achieving large strain deformation.[21] On the other hand, SCPs with SME have great stretchability, high elongation at break, and self-healing ability, but their deformation controllability is poorer than LCEs when used as photoactuators of soft robots.[22]

Herein, a new multifunctional programmable composite with a unique patch-sewing structure was designed and studied. In this system, a linear long molecular chain containing azobenzene served as a functional thread passing through the liquid crystal network, which made a distinguished balance between the response behavior and physical performance. The composite presented superior mechanical properties (tensile strength of 12.94 MPa, elongation at break of 274.84%) and artificial muscle performance (the energy density of 1.5332 kJ kg^{-1} is 46.5 times that of human skeletal muscles; the power density of 1330.53 W kg^{-1} is 26.6 times that of human skeletal muscles). Meanwhile, due to the introduction of azobenzene liquid crystal moieties[19] and gold nanorods,[23] the composite provided the basis for studying the mechanism of photoisomerism induced by ultraviolet (UV) and photothermal transformation triggered by near-infrared (NIR) light for artificial muscles with reversible cycles. After being prestressed at room temperature, the polymer-based composite bent and curled under the irradiation of 365 nm UV light in 29.3 s, and subsequently the shape recovery process could be realized under the irradiation of NIR light at 800−900 nm in 27.3 s, forming a reversible cycle. Besides, the rewriting ability based on self-healing performance has been observed at the second level (within 10 s). To study the mechanism of multiscale deformation, we performed the multiphysics finite element modeling of the photomechanical response with COMSOL Multiphysics to simulate the processes of the motion cycle based on Beer−Lambert's law,[24] and the results matched the experimental data precisely, which provided a general simulation framework and a numerical confirmation method for such photoinduced SMP actuators.

MATERIALS AND METHODS

Chemicals. Cetyltrimethylammonium bromide (CTAB) was purchased from Solarbio Technology Co. Ltd. A 4A molecular sieve was purchased from Energy Chemical Co. LTD. Dihydroxyl-terminated polycaprolactone (PCL-diOH) (M_n = 4000 g mol^{-1}) was obtained from the Shanghai D&B Laboratory. 4-Ethoxyaniline (≥98%), hydrochloric acid (HCl) (GR, 36−38%), sodium nitrite (GR), phenol (≥99.5%), sodium hydroxide (95%), 1-bromoundecane (98%), potassium iodide, potassium carbonate (GR), hexamethyltriphosphotriamine, ethyl alcohol (AR), sodium tetrahydroborate (>96%), chloroauric acid (>99.9%), silver nitrate, ascorbic acid, ditin butyl dilaurate, *N*,*N*-dimethylformamide (DMF) (>99.9%), ethyl acetate (AR), methylene dichloride (GR), petroleum ether (GR), and hexamethylene diisocyanate (HDI) (>98%) were purchased from Aladdin Chemical Reagent Co. Reagents were used as received unless specific instructions were given.

Synthesis of Monomers. For AZO-OH, 4-ethoxyaniline (3.45 g) and 36% HCl (8.52 mL) were first dissolved in deionized (DI) water (50 mL) under an icy bath with stirring constantly. Meanwhile, sodium nitrite (2.07 g) was dissolved in DI water (30 mL) and added into the solution drop by drop for at least an hour. Then, phenol (2.35 g) and sodium hydroxide (4.0 g) were dissolved in DI water (40 mL) and added into the mixture drop by drop for another hour. After that, some sodium hydroxide was added to adjust the pH to 10.0, and the mixture was stirred for another 3 h. At last, the mixture underwent suction filtration, and the remaining solid was recrystallized by the solution ($V_{\text{ethyl alcohol}}/V_{\text{ethyl acetate}}$ = 1:1), followed by drying in a vacuum oven. AZO-diOH could be obtained by similar preparation except for using *p*-aminobenzyl carbinol as the reagent. As for AZO11, AZO-OH (0.968 g), 1-bromoundecane (0.94 g), potassium iodide (0.05 g), potassium carbonate (1.656 g), and hexamethyltriphosphotriamine (0.05 g) were dissolved in ethyl alcohol (50 mL), and the reaction lasted for 2 days at 95 °C with strong stirring. Then, the mixture underwent suction filtration and the remaining solid was purified by silica column chromatography with a fluid phase ($V_{\text{methylene dichloride}}/V_{\text{petroleum ether}}$ = 1:1). At last, the obtained solid was dried in a vacuum oven. As for gold nanorods, the sodium borohydride solution (10 mM, 0.6 mL) was added dropwise rapidly into the mixture of chloroauric acid (0.5 mM, 5 mL) and CTAB (200 mM, 5 mL), followed by strong oscillation for 2 min and rested at 30 °C for 3 h to acquire the seed solution. Finally, CTAB (200 mM, 10 mL), DI water (10 mL), chloroauric acid (40 mM, 250 μL), silver nitrate solution (40 mM, 50 μL), 36% HCl (15 μL), ascorbic acid (100 mM, 160 μL), and the seed solution (500 μL) were poured into a conical flask in turns. After a rest for at least 3 days, the solution needed to be centrifuged at 10 000 rpm for 15 min three times to wash the surfactant, and the remaining solid was dried in a vacuum oven.

Fabrication of the Composites. PCL-diOH, HDI, AZO11, AZO-diOH, and gold nanorods were intensively dried by the 4A molecular sieve or vacuum drying overnight. A certain amount of AZO11, AZO-diOH, PCL-diOH, and gold nanorods were dissolved in DMF using ultrasonic oscillation for 10 min, and the mixture was stirred at 80 °C until it was clear. (Table S1) After that, HDI was added into the mixture, which was prior to the addition of ditin butyl dilaurate. When the mixture became sticky, which meant that the prepolymerization reaction had been completed, the mixture was transferred quickly to the preheated mold. After a 1 day reaction at 80 °C, the sample could be taken out with a scraper. Since the initial shape of as-synthesized composites could be devised by the geometry of the mold, different geometries could be achieved, for example, the film and fiber. It should be noted that the whole process should be in the nitrogen atmosphere because H_2O prevents the reaction from happening.

Physicochemical Characterization. Fourier transform infrared (FTIR) spectra of samples with different contents were obtained using a Nicolet 6700 (Thermo Fisher). UV−vis absorption spectra of gold nanorods and the composites were obtained by a Lamda 950 (PerkinElmer). Transmission electron microscopy (TEM) images of gold nanorods were taken with the TALOS F200X field emission transmission electron microscope (FEI). The microstructure and energy dispersive spectroscopy (EDS) mapping of the composite were observed by MIRA3 (scanning electron microscope, SEM) and Aztec X-MaxN80 (EDS) field emission scanning electron microscopes (TESCAN), respectively. The ^{1}H NMR spectra of the samples were acquired by the Avance III 400 MHz (Bruker). The spectra of ultraperformance liquid chromatography−mass spectrometer (LC−MS) were obtained by a UPLC and Q-TOF MS Premier (ACQUITYTM). The dynamic light scattering (DLS) result was tested by photon correlation spectroscopy (Zetasizer Nano S). The

https://dx.doi.org/10.1021/acs.chemmater.0c04170
Chem. Mater. 2021, 33, 987−997

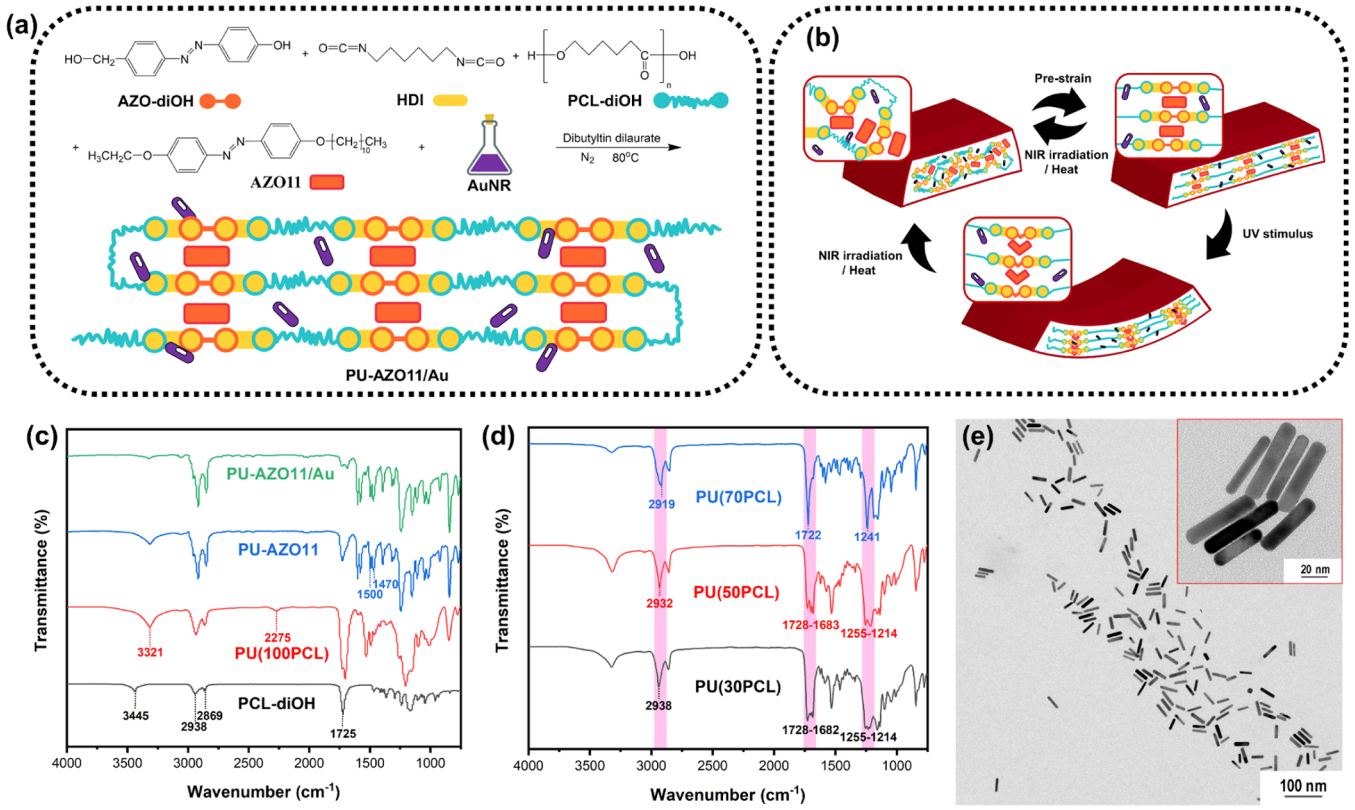

Figure 1. Structure and characterization of the multifunctional polymer composite for artificial muscle. (a) Schematic presentation of the synthetic route of composites with the designed structure as a functional thread passing through the liquid crystal network. (b) Schematic diagram of the three-step multiple stimulus-response cycle. (c) Comparison of FTIR spectra of PCL-diOH, PU(100PCL), PU-AZO11, and PU-AZO11/Au. (d) Comparison of FTIR spectra of composites with different PCL contents. (e) TEM image of gold nanorods with different scale bars.

gel permeation chromatography (GPC) curve was obtained from an ECS000113 (GPCEco).

Thermodynamic Characterization. The DSC curves were obtained using a Q2000 differential scan calorimeter (TA instruments) operated at a scanning rate of 10 °C min^{-1} under the nitrogen atmosphere. The dynamic mechanical analysis (DMA) analysis was carried out using a DMA 8000 (PerkinElmer) in 3-point bending mode at a heating rate of 3 °C min^{-1} at a constant frequency of 1 Hz. The X-ray diffraction (XRD) patterns were obtained by a D8 ADVANCE, (Bruker) with 2θ in the range of 5−70° with a step size of 5° min^{-1} from 25 to 120 °C at the heating rate of 1 °C min^{-1}. The polarizing microscopy (POM) images were observed by a DM LP (Leica) at the heating rate of 1 °C min^{-1}, and the test temperature was maintained for 10 min.

Tensile Testing. Mechanical tensile tests were performed with a universal tensile testing machine Z020 (Zwick Roell). Samples were initially prepared in a dumbbell shape mold with the geometry according to the standard type (170 mm × 20 mm × 3 mm) for the test with a reduced size of 85 mm × 10 mm × 1.5 mm. The strain rate was 10 mm min^{-1} and the precision of the temperature control component was 1.0 °C.

Shape Memory and Artificial Muscle Behavior. Samples were initially prepared in the dumbbell shape mold with the geometry with the reduced size of 4 mm × 5 mm × 0.5 mm. In terms of the shape-memory test, the sample was stretched in one direction to a 200% strain state at room temperature, which was regarded as the prestrain process. Then, the samples were put into water with a fixed temperature using tweezers, and the precision of the digital thermometer was 1.0 °C. As for the artificial muscle test, the samples were fixed vertically on the iron platform, and clamps were used to connect the load to the samples (the weight of the clip is 2.9525 g).

Rewriting and Photoresponse Performance. Rectangular 40 mm × 40 mm polymer films were prepared initially and cut into desired shapes such as strips for the test. A xenon lamp light source used in the test was obtained from Shanghai Yuming Instrument Co., Ltd. with a bulb power of 300 W and the maximum current of 22 A. The filter used in the UV test experiment was a 365 nm band while the band between 800 and 900 nm was used in the NIR response test.

Computational Methods and Models. COMSOL Multiphysics 5.4 was used to solve the light absorption and mechanical deformation. The material parameters used were from the sample PU-5AZO11/Au(50PCL), as shown in Table S1, with a thickness of 0.1 mm.

RESULTS AND DISCUSSION

As seen in Figure 1a, the formation and the fundamental structure of the composite PU-AZO11/Au could be presented clearly as a linear azobenzene-contained copolymer with the gold nanorods dispersed in the liquid crystal network. For the procedure of synthesis, 4-ethoxyaniline and *p*-aminobenzyl alcohol (*p*-ABA) were selected as the reagents and designed to be converted into liquid crystal elements (AZO-diOH and AZO11) by the diazo-reaction (Scheme S1a,b). The main polymer chain was obtained by the reaction between the isocyanate and hydroxyl groups. In this step, AZO-diOH, hexamethylene diisocyanate (HDI), polycaprolactone terminated by double hydroxyl (PCL-diOH), and dibutyltin dilaurate functioned as the liquid crystal segment, chain extender, soft segment, and catalyst for condensation polymerization, respectively (Scheme S1c). On the other hand, the gold nanorods as the significant photothermal conversion particles for the system were prepared based on El-Sayed's method utilizing chloroauric acid, sodium borohydride, and silver nitrate (Scheme S2a).[25] To acquire the oil-soluble gold

https://dx.doi.org/10.1021/acs.chemmater.0c04170
Chem. Mater. 2021, 33, 987−997

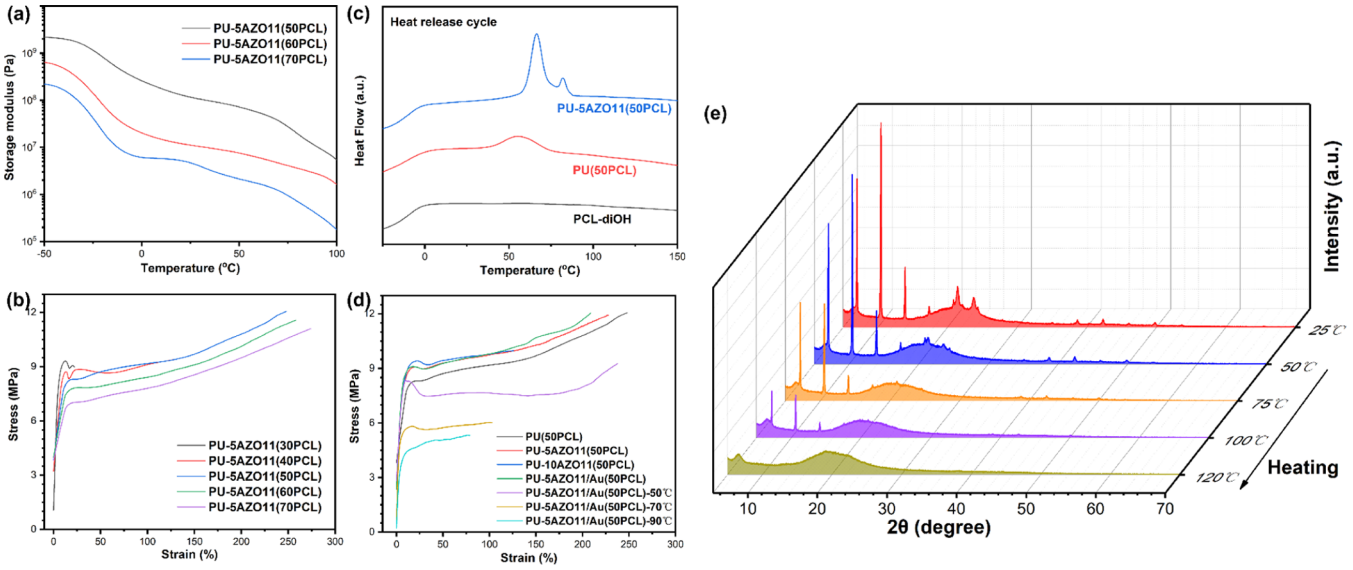

Figure 2. Thermal and mechanical behavior of the multifunctional polymer composite for artificial muscle. (a) DMA diagrams of the composite PU-5AZO11 with different PCL contents. (b) DSC curves of PCL-diOH, PU(50PCL), and PU-5AZO11(50PCL) in a heat release cycle. (c) Stress−strain diagrams of the composite PU-5AZO11 with different PCL contents. (d) Heating stress−strain diagrams of composites with different AZO11 and Au contents. (e) One-dimensional XRD patterns of the composite PU-5AZO11/Au(50PCL) under the heating circumstance.

nanorods that could react in the organic solvent for being integrated into the polymer, further processes were considered, such as centrifugation and ultrasonication (Scheme S2b). The composite material was in situ polymerized by casting the mixture solution into the self-made polytetrafluoroethylene (PTFE) molds directly under the nitrogen atmosphere (Scheme S3). The PCL-diOH reagent, a colorless liquid with a certain viscosity under the temperature for prepolymerization, could react perfectly with the *N*,*N*-dimethylformamide (DMF) solution of HDI and AZO-diOH to generate the linear long molecular chain, which served as a functional thread passing through the liquid crystal network. Because of the $\pi-\pi$ interaction existing in the similar azobenzene structure between AZO-diOH and AZO11,[26] a novel patch-sewing structure liquid crystal nanocomposite network PU-AZO11/Au could be realized, as shown in Figure 1a. Pure polyurethane made with PCL-diOH and HDI was too soft to support itself, and the increasing amount of azobenzene groups served as the hard segments, which strengthened the mechanical properties of the composite to provide the mechanical basis for the photoisomerization and photothermal behavior (Figure 1b).

As presented in Fourier transform infrared (FTIR) spectra (Figures S1 and S2), the azobenzene group peaked at 1499 and 1474 cm^{-1} while the double peaks at 3425 and 3354 cm^{-1} were associated with the aniline group, and there was an obvious peak at 3336 cm^{-1} referring to the hydroxyl group. The conversion of the aniline group to the hydroxyl group and the appearance of the azobenzene group indicated the success of the diazo-reaction. For the next step, the vanishing hydroxy group and the remaining azobenzene group accounted for the alkylation reaction. On the other hand, from the spectrum in Figure 1c, which demonstrated the success of polymerization, absorption at 2938 and 2869 cm^{-1} corresponded to the -CH2- symmetric and asymmetric vibrations, respectively. Due to the existence of the C−O bonds from PCL, there was an obvious peak at the 1725 cm^{-1}. As the reaction continued, a single peak representing the amino bond in the urethane group at 3321 cm^{-1} and a double peak suggesting the azobenzene group at 1470−1500 cm^{-1} appeared, while the peak at 3445 cm^{-1} referring to the hydroxy group disappeared, which indicated the achievement of condensation polymerization among all kinds of samples. Since the HDI in the composites was excessive, a small amount of -NCO bonds might exist, peaking at 2275 cm^{-1}. Additionally, as shown in Figure 1d, with the increase of the azobenzene content, the single peak referring to the benzene ring (1722 and 1241 cm^{-1}) turned into a broad peak, because the intermolecular forces caused the change of the chemical environment of the benzene ring. Meanwhile, the $\pi-\pi$ interaction of the patch-sewing structure was beneficial to homogenize and stabilize the electron cloud, which resulted in the red shift of the C−H vibration peak from 2919 to 2938 cm^{-1}.[27]

The chemical structure could be further substantiated using a nuclear magnetic resonance (^{1}H NMR) spectrometer (Figures S3−S7) and an ultraperformance liquid chromatography-quadruple time-of-flight mass spectrometer (LC−MS) (Figures S8−S10), from which all of the target contents could be calculated to be more than 99.9% after integration and the contrast with the background. As for the other significant components of the system, gold nanorods grew with homogeneous dispersion, and the average length was approximately 60 nm, as shown in Figure S11, while the peak at 3.344 nm referred to a small number of seed grains through dynamic light scattering. As could be verified from Figure S12, compared with the nanospheres, due to the surface plasmon resonance effect,[28] the main absorption peak of the prepared gold nanorods was shifted from 550 to 850 nm, which was exactly in the NIR response zone. By means of analyzing the ultraviolet-visible (UV−vis) spectrum in Figure S13, the gold nanorods were well integrated into the system possessing a similar absorption with the solution. To be more specific, the transmission electron microscopy (TEM) image precisely presented the morphological features of gold nanorods with the aspect ratio of 7:1 (Figure 1e). It is worth mentioning that the gold nanorods had been successfully transferred from a water-based solvent to an oil-based solvent

https://dx.doi.org/10.1021/acs.chemmater.0c04170
Chem. Mater. 2021, 33, 987−997

and finally into the composite without any obvious change through the process (Figure S14). Furthermore, the homogeneously stable composites without any defect could be observed in the scanning electron microscopy images (SEM), and the analysis by energy-dispersive spectroscopy (EDS) spectra revealed that each component including gold nanorods was dispersed uniformly as designed (Figure S15), which was also determined by gel permeation chromatography (GPC) with a narrow molecular weight distribution of 1.166 (Figure S16).

The thermodynamic properties of composite PU-AZO11/Au are influenced by the microphase separation, hydrogen bonding, and orientation. First and foremost, in terms of the molecular structure and configuration, elastomer PU is generally a kind of block polymer consisting of soft and hard segments, and there is no exception for this novel design. Among them, the long-chain PCL, acting the role of the soft segment, presents a state of the random alignment because of numerous conformations at room temperature. In the meantime, these soft segments tend to gather together to form soft segment microareas. On the other side, the urethane structure obtained by the polymerization of HDI and AZO-diOH constitutes hard segments. In contrast to soft segments, hard segments are relatively stiff and form the rigid rod shape whose conformation is not easy to collapse at room temperature. The $\pi-\pi$ interaction of the benzene ring and the hydrogen bonds between the molecular chains are associated together as hard segment microregions that crystallize at room temperature. Because the hard segment is distributed in the soft segment instead of dissolving in it, it serves as a physical cross-linking point in the system. Meanwhile, the structural disparity, which contributes to the difference in thermodynamic and the high cohesive energy of the polar groups such as urethane groups, results in the formation of associated microdomains and microphase separation, bringing about the influence of thermal and mechanical properties.[29]

As presented in the dynamic mechanical analysis (DMA) curves (Figure 2a), along with the increase of PCL as the soft segment in the system from 50 to 70 wt %, a moderate drop of the glass transition temperature (T_g) could be found from −2.41 to −14.89 °C, which was identified with the tan delta (Figure S17). There existed a percentage growth of the PCL component with a large amount of amorphous phase so that the melting point (T_m) declined from 68.40 to 60.10 °C (Table S1). Besides, a tensile test in stress−strain measurements was conducted at room temperature, where Young's modulus (E) fell from 205.34 to 143.92 MPa steadily, and the elongation at break (ε_B) climbed from 13.92 to 274.84% when the content of PCL increased from 30 to 70 wt % (Figure 2b). An important phenomenon was that if the proportion of PCL was lower than 30%, the prepared sample would exhibit the hard and brittle properties. When the percentage of PCL reached 50%, the composite PU-5AZO11 behaved as a typical crystalline polymer with obvious strain softening and necking. The same graph offered a glimpse of a gradual rise of the breaking elongation and the breaking modulus (σ_B) peaks at 12.06 MPa owing to the substantial microphase separation based on the balance between the hard and soft segments.

Secondly, AZO11, the liquid crystal enhancement, demonstrated prominent thermal response ability, which could be proved by differential scanning calorimetry (DSC) analysis, as shown in Figure S18, where a sharp peak at 99.49 °C was for T_m and the other one at 111.62 °C was for the liquid crystal clearing point (T_{cp}) through a heating−releasing cycle. The same test conditions were set for samples with 5 wt % contents of AZO11. These results illustrated that the combination of polyurethane and the AZO11 liquid crystal network contributed two critical transition temperatures, which were between the T_m of pure polyurethane and AZO11 (Figures 2c and S19). In the matrix, the hard segment with the imino group has proton donors, while both the hard and soft segments have carbonyl groups as proton acceptors, which generate a mass of hydrogen bonds.[30] With an increase of the content of AZO11 containing considerable ether bonds and benzene rings, the strength of the composites continually enhances, which relies on the impact of hydrogen bonding and the $\pi-\pi$ stacking effect that plays a non-negligible role in physical cross-linking (Figure S20). At the macroscopic scale, the stress−strain curves demonstrated that AZO11 was beneficial to the strength to a certain extent, and over 10 wt % of it can make the composites brittle. When the test temperature reached 50 °C, the soft segment in the composite showed a partial melting tendency, resulting in a drop of σ_B to 75.19% at room temperature. There was a conspicuous slump of mechanical properties such as E, σ_B, and ε_B as the temperature rose further and turned into the viscous state eventually (Figure 2d), which corresponded to the DMA diagrams (Figure S21).

As the last point for orientation, with the addition of the liquid crystal reinforcement, there are several types of orientation in the system so as to improve the strength of the prepared elastomer. In addition to the orientation of azobenzene between the adjacent hard segments and liquid crystal phase, the orientation resulting from partial crystallization between PCL soft segments could be verified from X-ray diffraction (XRD) patterns obtained after heating them (Figure 2e).[31] At room temperature, the soft segments displayed diffraction patterns in the Bragg equation of 21.9 and 24.1° due to their orthorhombic structure while the narrow peaks of 6.90, 10.33, and 13.88° referred to the liquid crystal elements.[3] When the testing temperature was over the melting point of the PCL segment, the corresponding crystals disappeared. Similarly, since the sample was heated up to more than 110 °C, which was the clearing point of AZO11, the only broad peak left was caused by the organic matrix. This two-stage crystallization could reappear during the reversible cycle, which brought into correspondence with the polarizing microscopy (POM) images, as shown in Figure S22. Moreover, as shown in Figure S23, the degree of crystallinity and orientation of the composites increased with the growth of the content of AZO11.

Since the effect of phase separation and physical interaction, shape-memory performance can be realized, which is assessed by two decisive parameters, the shape fixation ratio (R_f) and the shape recovery ratio (R_r). They represent the capabilities of the materials to maintain the deformation state and return to the original state, respectively. These two parameters can be calculated from eqs S1 and S2 (Supporting Information Supplementary 1). For the convenience and accuracy of comparison, the test samples were all specified that L_1 was twice as much as L_0, that is, the shape-memory performance was tested under the conditions of 100% strain. The results demonstrated that all of the samples presented nearly 100% R_f, which indicated that the copolymer system could be changed and fixed controllably. As the temperature increased, the

https://dx.doi.org/10.1021/acs.chemmater.0c04170
Chem. Mater. 2021, 33, 987−997

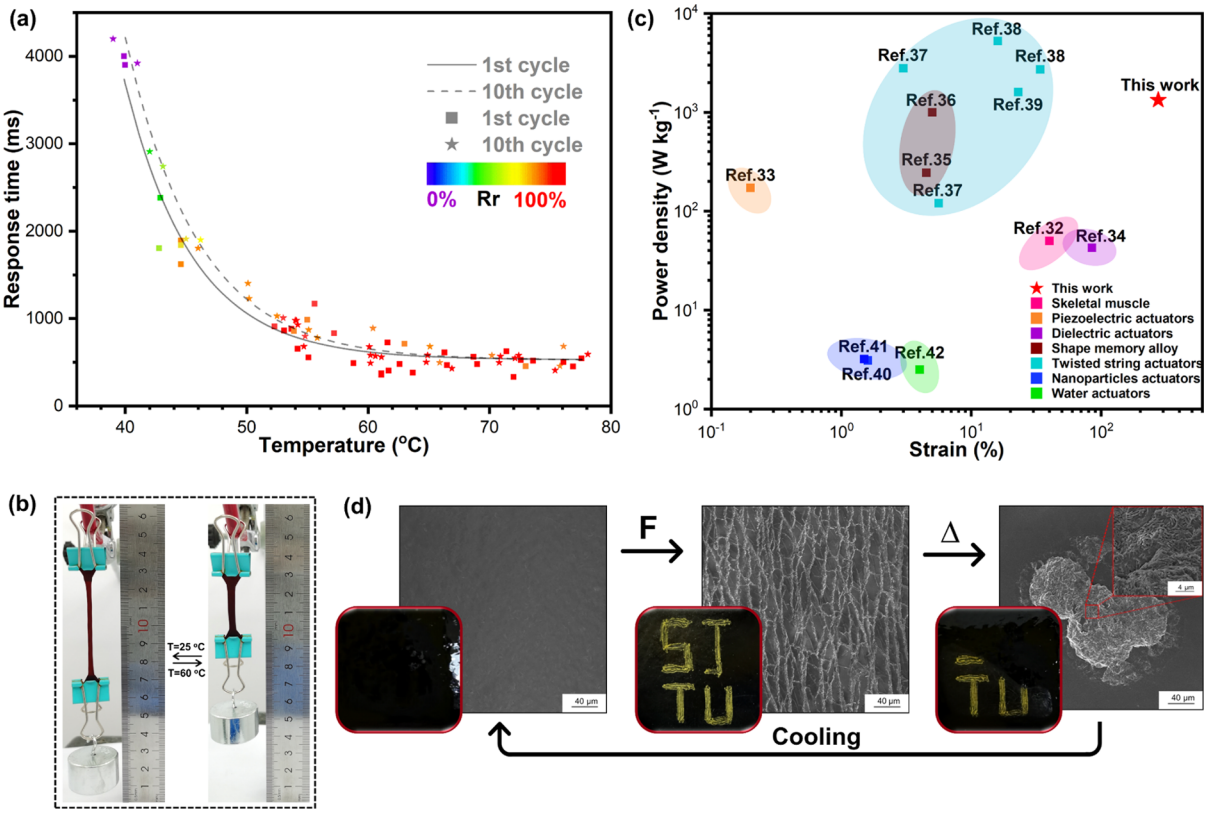

Figure 3. Artificial muscle performance and rewriting behavior of the composite PU-5AZO11/Au(50PCL). (a) Performance of the 1st and 10th cycles of the composite at varied temperatures (R_r is represented by the color, red for 100%, purple for 0%). (b) Schematic diagram of a classical lifting application to test the artificial muscle performance. (c) Comparison of artificial muscle performance with other common actuator materials. (d) Optical images and SEM images of the rewriting performance of PU-5AZO11/Au(50PCL) in the original, scratched, and healing states. (F is for external force, Δ is for heating).

response time of the sample continually decreased and R_r gradually approached 100% (Videos S1 and S2). Given that the T_m of the PCL component was 53.37 °C, which could trigger the recovery behavior, the values of R_r and response time were significantly different before and after this critical temperature, as shown in Figure 3a. It is worth noticing that the deformation would be well fixed in the environment of 40 °C and below when the composite was released from the external force at room temperature, while it could instantaneously restore when the temperature reached 60 °C and above. In addition, when the samples underwent 10 cycles of shape-memory tests, their overall properties almost remained the same except that R_r became 90−95%. This phenomenon indicated that this material had promising potential in applications such as artificial muscles. This was further proved by the crane-like lifting test, as shown in Figure 3b. Along with loading, the experimental results were consistent with those of previous testing (Video S3). There was no difficulty in finding that a large amount of heat could activate the system to release the prestored entropy energy under the 60 °C environment, consequently driving the sample to shrink to its initial state, the most stable state with the largest entropy.[13]

It could be observed that this kind of composite PU-5AZO11/Au(50PCL) (the mass of the deformation section was 0.025 g) could easily lift a load of more than 2000 times its own mass (52.9528 g). As the weight continued increasing and exceeded the entropy energy of the system, it reached the load limit of the material, so that the material could not fully recover (Video S4). As exhibited in Video S5, the sample could come up to the critical temperature immediately by employing a heating gun, which could achieve rapid recovery. The energy density (W) and power density (P) can be calculated from eqs S3 and S4 (Supporting Information Supplementary 1). The energy density of this material was up to 1.5332 kJ kg^{-1}, and the average power density was 1330.53 W kg^{-1} after calculation (Table S2). In contrast to some common types of artificial muscle actuators,[32−42] this material had an outstanding balance between the energy density and strain, which meant that it demonstrated the super-extendable performance, as well as unparalleled energy density and power density. Specifically, the maximum strain was 6.9 times that of human skeletal muscles, while the power density was 26.6 times, and the energy density was 46.5 times (Figure 3c).[43] Similarly, after the cyclic test of 10 times, the main parameters remained unchanged and R_r only dropped by 2.31%, which displayed a remarkable comprehensive performance for artificial muscles.

To our surprise, at the temperature of over 100 °C, the composite exhibited self-healing properties on the surface, which enabled a rewriting behavior (Video S6). This phenomenon can be explained by two reasons. First, the physical forces, including the $\pi-\pi$ interaction and hydrogen bonding interaction in the system, can reconstruct the surface and heal the cracks. In the meantime, as the temperature rises, the components of PCL and AZO11 in the composite start to melt, which results in the increase of mobility of chains. Due to the physical interaction in the system and the presence of chemical cross-linking, these components will not be detached

https://dx.doi.org/10.1021/acs.chemmater.0c04170
Chem. Mater. 2021, 33, 987−997

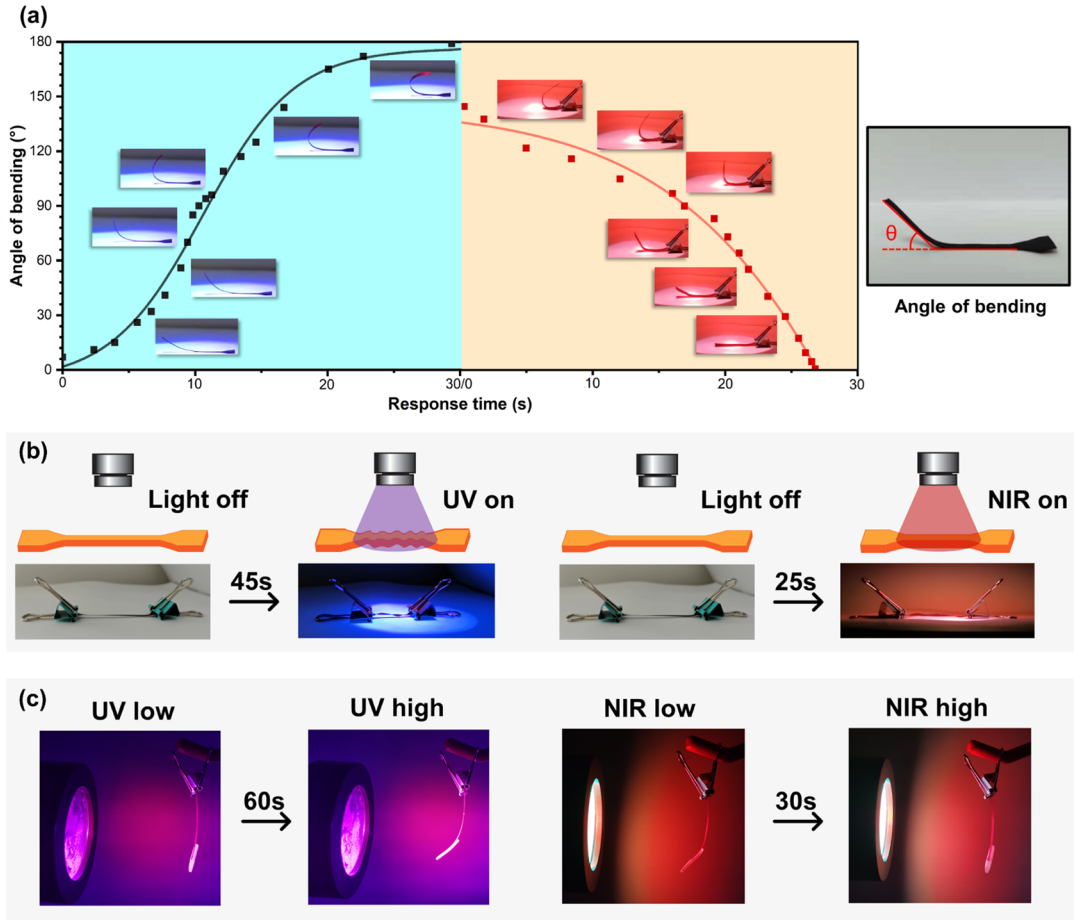

Figure 4. Photoresponsive behavior of the composite PU-5AZO11/Au(50PCL). (a) Cycle of bending induced by UV at 365 nm and recovery induced by NIR 800−900 nm of the prepared composite strip with one end fixed. (b) Schematic diagram and corresponding images of the light-driven application. (c) Artificial muscle performance triggered by UV at 365 nm and NIR 800−900 nm.

and tend to rearrange and reorient to form a flat surface instead, as shown in SEM images in Figure 3d. Moreover, as shown in Figure S25, when the content of AZO11 was 2.5 wt %, the handwriting was hard to be observed because the $\pi-\pi$ and hydrogen bonding interactions were strong enough to keep AZO11 in the composites so that PU-2.5AZO11/Au(50PCL) did not present the self-healing behavior. As for samples with more AZO11 (≥5 wt %), there was no difficulty finding the scratched area because the weight ratio of AZO11 reached the critical value, resulting in the separation of part of AZO11. After the approximately 1 min heating process, PU/Au(50PCL) with 5.0, 7.5, and 10.0 wt % could heal their surfaces because the melting AZO11 reflowed in the scratched area. However, when the temperature decreased, as the weight ratios increased, AZO11 molecules tended to crystallize and aggregate at the surface to generate a spherical morphology. After many comparisons, PU-5AZO11/Au(50PCL) was considered to have the optimum performance, as shown in Figure S25c. This behavior will be beneficial for recording the deformation of the materials, which is probably advantageous to artificial muscle applications like an alarming apparatus.

Because of the introduction of azobenzene and gold nanorods, the composite has achieved a dual response to UV and NIR light. As for the UV response, the azobenzene group is a trans rod-like molecule under thermally stable conditions, while it turns into the cis V-shaped molecule under UV irradiation around the 365 nm wavelength. This photo-isomerization effect shortens every group of azobenzene from 9.0 to 5.5 Å. It will be stored in the long molecular chain, and the accumulated internal stress will cause macroscopic bending deformation towards the UV light.[19] On the other hand, due to the plasmon resonance effect on the surface, nanocrystals of Au can absorb a huge amount of light energy from NIR and release it as thermal energy.[44] By adjusting the ratio of raw materials to control the length−diameter ratio of the nanorods, the absorption peak of the composite was located at 800−900 nm.[25]

As shown in Figure 4a, when the composite PU-5AZO11/Au(50PCL) with one end fixed was exposed to UV light, with the help of AZO11 to activate azobenzene in the backbone, the bending angle between the two ends could be 180° in 29.3 s. Due to the effect of gravity and change of the radiation area, the response curve presented an S-shaped growth, and the deformation could be fixed eventually (Video S7). Subsequently, the light source was switched to NIR irradiation, and the sample showed a fast recovery to its initial state within 27.3 s (Video S8). The given curve indicated an acceleration of deformation, resulting from the increase of the radiation area and heat conduction.

Furthermore, drive experiments were conducted and each composite strip with 100% strain was applied by two clips with a weight of 2.9525 g each (approximately 300 times the mass of the sample), as shown in Figure 4b. Since the two ends were fixed by the load, the isomerization triggered by UV light

https://dx.doi.org/10.1021/acs.chemmater.0c04170
Chem. Mater. 2021, 33, 987−997

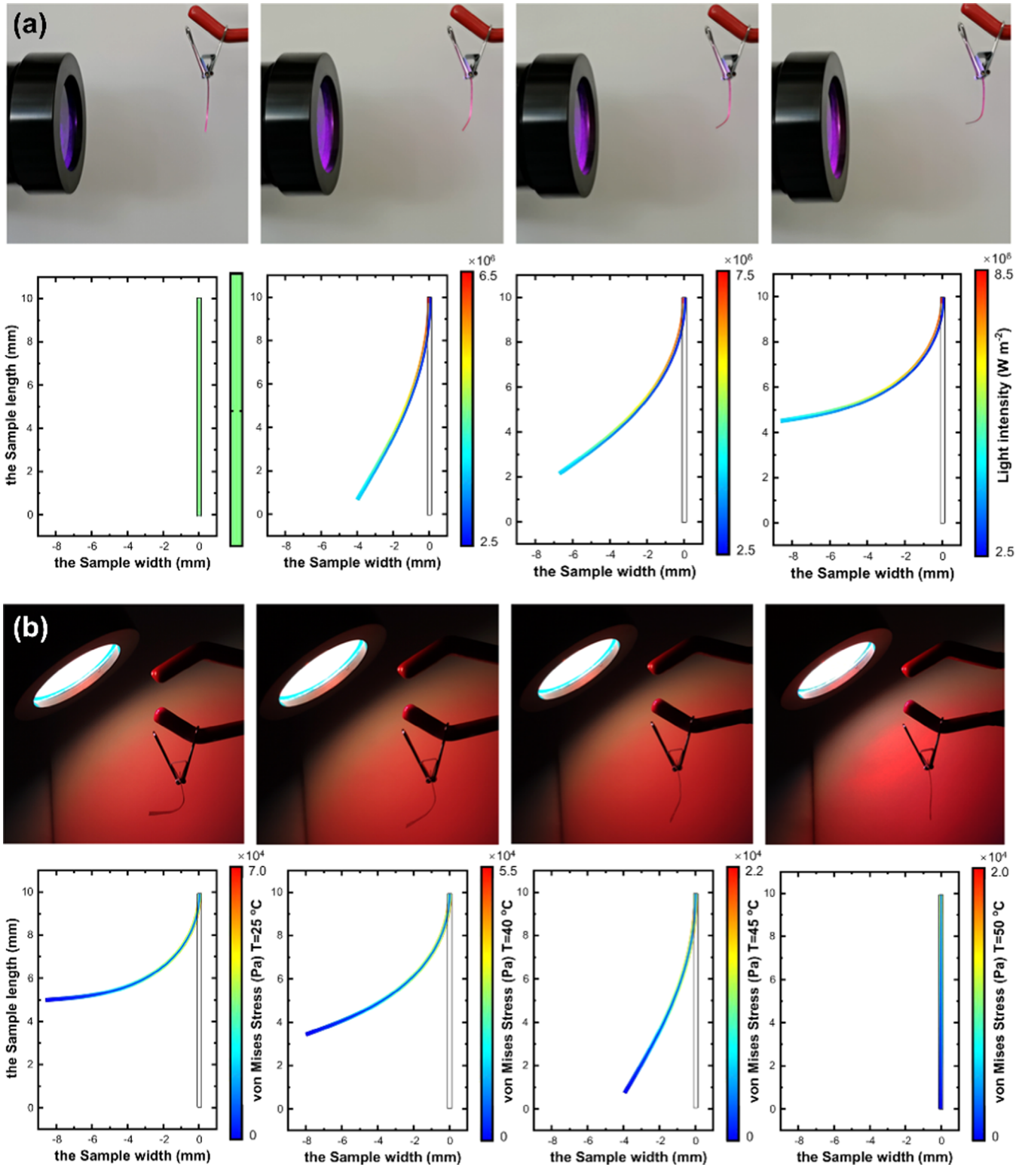

Figure 5. Simulation results of the finite element model and experimental results of the prepared composite strip PU-5AZO11/Au(50PCL) with one end fixed under (a) UV and (b) NIR irradiation, respectively.

caused the sample to shrink and twist instead of bending, leading to the 14% strain state in 45 s (Video S9). In contrast, the NIR-driven behavior exhibited higher power and efficiency. Under the same conditions, it only took 25 s to achieve a complete recovery. To imitate the natural muscle behavior, one end of the composite strip (0.0155 g) was fixed vertically after preorientation while the other end was attached to the load (0.1280 g), as shown in Figure 4c. Under the UV light, PU-5AZO11/Au(50PCL) could drive a load of more than 8.3 times its own mass to achieve a 60° bending in 60 s. When the light source was switched to NIR, the recovery process was activated and the bending angle returned to its original state within 30 s, which was consistent with the result of drive experiments. Compared with thermal initiation, the driving

https://dx.doi.org/10.1021/acs.chemmater.0c04170
Chem. Mater. 2021, 33, 987−997

ability of light is relatively small because the efficiency of isomerization and the photothermal energy conversion is significantly lower than that of heat. Yet, this phenomenon was still noteworthy, as it was rarely reported in other light-driven soft materials for bending with the load.[19,45,46]

To study and understand the mechanism of the macroscopic deformation, we performed a finite element analysis-based simulation of the light response of azobenzene groups and gold nanorods based on Beer−Lambert's law. The photomechanical behavior involves multiscale mechanics, including the force field, thermal field, and optical field. At the microscale, the specific light irradiation will trigger isomerization reactions of the azobenzene moiety, which leads to deformation at the macroscopic scale. This trans-to-cis isomerization of azobenzene was modeled with molecular dynamics (MD) simulation.[47] Then, by utilizing the micromechanics-based homogenization method, the effective elastic properties of elastomers were numerically derived with respect to the isomerization ratio,[48] and the microscopic behavior was transduced to the macroscopic deformation.[49] Finally, the macroscale photomechanical response of the composites was simulated by finite element analysis, where the effective mechanical properties were usually identified numerically by matching the FE model with the MD model. Herein, we modeled the macroscopic deformation of a two-dimensional straight cantilever beam in response to UV and NIR light excitation.[50] In the simulation of the UV response, we used the Radio Frequency package to solve the electromagnetic problem of light scattering and absorption. To efficiently model the light excitation, a steady-state plane wave (with a certain wavelength and light intensity) from one side of the sample was set. The light absorption was then evaluated by Beer−Lambert's law.[24] For the next step, the Structural Mechanics package was adopted to calculate the corresponding material deformation of the two-dimensional cantilever by introducing an equation that expressed the light-induced strain as a function of the retrieved light intensity. Then, the macroscopic photomechanical response (the light-induced deformation, strain, and stress) was simulated by this approach.

As shown in Figure 5a, since the light intensity increased from 6.5 to 8.5 W m^{-2}, the incidence of azobenzene isomerization in the system continued to rise, especially on the opposite side of the light source, which led to UV phototaxis. In the NIR response simulations, we used the Heat Transfer package and the Solid Mechanics package to model the heat recovery process. We made a certain simplification here that we directly set the temperature in the outer boundary of the sample. However, the heat converted from the NIR could also be simulated with the Radio Frequency package. The results proved that gold nanorods transformed NIR energy into thermal energy continuously through photothermal conversion, which raised the temperature of the sample. When it reached the transition temperature, the molecular mobility was reactivated, allowing the system the return to its highest entropy state so that the entropy of the system caused by an external force in the prestrain process was being released. Therefore, the shape recovery process would be triggered, as shown in Figure 5b. Overall, the results of the simulation exactly matched the experimental results, which offered a general method to study light-driven elastomers induced by both UV and NIR irradiation.

CONCLUSIONS

In summary, we have developed a novel multifunctional programmable nanocomposite with a unique patch-sewing structure, which showed a remarkable shape-memory behavior and outstanding artificial muscle performance. Owing to the effects of the microphase separation, the $\pi-\pi$ interaction, and hydrogen bonding, the composite PU-AZO11/Au could be easily deformed and achieve a nearly 100% shape recovery ratio after 10 cycles and an instantaneous response within 1 s over the critical temperature. Furthermore, through the lifting experiment, the distinguished driving performance with 46.51 times the energy density, 26.6 times the power density, and 6.9 times the strain of human skeletal muscles could be overserved. Because of the addition of the AZO11, the rewriting behavior could be realized, resulting from the self-healing properties on the surface at 100 °C. Meanwhile, on account of the photoisomerization of azobenzene and the photothermal conversion of the gold nanorods, the cycle of triggering by ultraviolet and restoring by NIR light within 30 s could be accomplished. Moreover, we established the corresponding numerical model to simulate the movement induced by light and summarized the general laws of light-driven elastomers based on isomerization and photothermal conversion. These demonstrations clearly indicated that this innovative nanocomposite was promising for artificial muscle applications in numerous fields, such as soft robots and intelligent skin.

ASSOCIATED CONTENT

Supporting Information

The Supporting Information is available free of charge at https://pubs.acs.org/doi/10.1021/acs.chemmater.0c04170.

Shape-memory behavior and artificial muscle performance test; synthetic routes; FTIR spectra; ^{1}H NMR spectra; LC−MS results; DLS curve; UV−vis absorption spectra; TEM images; SEM images; EDS analysis; GPC curve; DMA diagrams; DSC curves; POM images; and tables with various mechanical and response properties of composites (PDF)

Shape recovery behavior induced by heat at 60 °C; (the movie is shown with a 1.0 × speed) (Video S1) (MP4)

Shape-memory performance at different temperatures; (the movie is shown with a 0.1 × speed) (Video S2) (MP4)

Artificial muscle performance at room temperature and over the critical point; (the movie is shown with a 1.0 × speed) (Video S3) (MP4)

Artificial muscle performance over the critical temperature with the varied load; (the movie is shown with a 1.0 × speed) (Video S4) (MP4)

Artificial muscle performance through 10 cycles; (the movie is shown with a 0.1 × speed) (Video S5) (MP4)

Rewriting performance induced by heat at 100 °C; (the movie is shown with a 2.0 × speed) (Video S6) (MP4)

Photoresponse performance induced by UV at 365 nm with one end fixed; (the movie is shown with a 1.0 × speed) (Video S7) (MP4)

Photoresponse performance induced by NIR at 800−900 nm with one end fixed; (the movie is shown with a 1.0 × speed) (Video S8) (MP4)

Photoresponse performance fixed induced by UV at 365 nm with both ends fixed; (the movie is shown with a 1.0 × speed) (Video S9) (MP4)

https://dx.doi.org/10.1021/acs.chemmater.0c04170
Chem. Mater. 2021, 33, 987−997

Photoresponse performance fixed induced by NIR at 800−900 nm with both ends fixed; (the movie is shown with a 1.0 × speed) (Video S10) (MP4)

AUTHOR INFORMATION

Corresponding Authors

Yujie Chen − *State Key Laboratory of Metal Matrix Composites, School of Materials Science and Engineering, Shanghai Jiao Tong University, Shanghai 200240, China;* orcid.org/0000-0003-2513-7559; Email: yujiechen@sjtu.edu.cn

Hezhou Liu − *State Key Laboratory of Metal Matrix Composites, School of Materials Science and Engineering, Shanghai Jiao Tong University, Shanghai 200240, China;* orcid.org/0000-0002-3521-1970; Email: hzhliu@sjtu.edu.cn

Authors

Chi Chen − *State Key Laboratory of Metal Matrix Composites, School of Materials Science and Engineering, Shanghai Jiao Tong University, Shanghai 200240, China*

Yangyuanchen Liu − *University of Michigan-Shanghai Jiao Tong University Joint Institute, Shanghai Jiao Tong University, Shanghai 200240, China*

Ximin He − *Department of Materials Science and Engineering, University of California, Los Angeles, Los Angeles, California 90095, United States;* orcid.org/0000-0001-8845-4637

Hua Li − *State Key Laboratory of Metal Matrix Composites, School of Materials Science and Engineering, Shanghai Jiao Tong University, Shanghai 200240, China;* orcid.org/0000-0003-2852-4722

Ying Wei − *College of Engineering and Applied Sciences, Nanjing University, Nanjing 210046, China*

Yusen Zhao − *Department of Materials Science and Engineering, University of California, Los Angeles, Los Angeles, California 90095, United States*

Yanfei Ma − *Department of Materials Science and Engineering, University of California, Los Angeles, Los Angeles, California 90095, United States*

Zhen Chen − *State Key Laboratory of Metal Matrix Composites, School of Materials Science and Engineering, Shanghai Jiao Tong University, Shanghai 200240, China*

Xu Zheng − *State Key Laboratory of Metal Matrix Composites, School of Materials Science and Engineering, Shanghai Jiao Tong University, Shanghai 200240, China*

Complete contact information is available at: https://pubs.acs.org/10.1021/acs.chemmater.0c04170

Author Contributions

All authors have given approval to the final version of the manuscript.

Notes

The authors declare no competing financial interest.

ACKNOWLEDGMENTS

This work was supported by the Natural Science Foundation of China (NSFC) (grant numbers U1733130 and 11704244); Joint Fund of the Education Ministry of China (grant number 6141A02022264); and Medical-Engineering Cross Research Funding of SJTU (grant numbers YG2017MS01 and YG2016QN34).

REFERENCES

(1) Mirvakili, S. M.; Hunter, I. W. Artificial Muscles: Mechanisms, Applications, and Challenges. *Adv. Mater.* **2018**, *30*, No. 1704407.

(2) Chen, S. E.; Cao, Y. T.; Sarparast, M.; Yuan, H. Y.; Dong, L. X.; Tan, X. B.; Cao, C. Y. Soft Crawling Robots: Design, Actuation, and Locomotion. *Adv. Mater. Technol.* **2020**, *5*, No. 1900837.

(3) Chen, Y.; Zhao, H.; Mao, J.; Chirarattananon, P.; Helbling, E. F.; Hyun, N.-S. P.; Clarke, D. R.; Wood, R. J. Controlled flight of a microrobot powered by soft artificial muscles. *Nature* **2019**, *575*, 324−329.

(4) Lu, X.; Guo, S.; Tong, X.; Xia, H.; Zhao, Y. Tunable Photocontrolled Motions Using Stored Strain Energy in Malleable Azobenzene Liquid Crystalline Polymer Actuators. *Adv. Mater.* **2017**, *29*, No. 1606467.

(5) Wehner, M.; Truby, R. L.; Fitzgerald, D. J.; Mosadegh, B.; Whitesides, G. M.; Lewis, J. A.; Wood, R. J. An integrated design and fabrication strategy for entirely soft, autonomous robots. *Nature* **2016**, *536*, 451−455.

(6) Miriyev, A.; Stack, K.; Lipson, H. Soft material for soft actuators. *Nat. Commun.* **2017**, *8*, No. 596.

(7) Zhang, B. W.; Jiao, Y.; Chao, D. L.; Ye, C.; Wang, Y. X.; Davey, K.; Liu, H. K.; Dou, S. X.; Qiao, S. Z. Targeted Synergy between Adjacent Co Atoms on Graphene Oxide as an Efficient New Electrocatalyst for Li-CO2 Batteries. *Adv. Funct. Mater.* **2019**, *29*, No. 1904206.

(8) Hia, I. L.; Vahedi, V.; Pasbakhsh, P. Self-Healing Polymer Composites: Prospects, Challenges, and Applications. *Polym. Rev.* **2016**, *56*, 225−261.

(9) Hu, L.; Wan, Y.; Zhang, Q.; Serpe, M. J. Harnessing the Power of Stimuli-Responsive Polymers for Actuation. *Adv. Funct. Mater.* **2019**, *31*, No. 1806386.

(10) Behl, M.; Kratz, K.; Zotzmann, J.; Noechel, U.; Lendlein, A. Reversible Bidirectional Shape-Memory Polymers. *Adv. Mater.* **2013**, *25*, 4466−4469.

(11) Ula, S. W.; Traugutt, N. A.; Volpe, R. H.; Patel, R. R.; Yu, K.; Yakacki, C. M. Liquid crystal elastomers: an introduction and review of emerging technologies. *Liq. Cryst. Rev.* **2018**, *6*, 78−107.

(12) Turner, S. A.; Zhou, J.; Sheiko, S. S.; Ashby, V. S. Switchable Micropatterned Surface Topographies Mediated by Reversible Shape Memory. *ACS Appl. Mater. Interfaces* **2014**, *6*, 8017−8021.

(13) Zare, M.; Prabhakaran, M. P.; Parvin, N.; Ramakrishna, S. Thermally-induced two-way shape memory polymers: Mechanisms, structures, and applications. *Chem. Eng. J.* **2019**, *374*, 706−720.

(14) Gao, H.; Li, J.; Zhang, F.; Liu, Y.; Leng, J. The research status and challenges of shape memory polymer-based flexible electronics. *Mater. Horiz.* **2019**, *6*, 931−944.

(15) Gelebart, A. H.; Mulder, D. J.; Varga, M.; Konya, A.; Vantomme, G.; Meijer, E. W.; Selinger, R. L. B.; Broer, D. J. Making waves in a photoactive polymer film. *Nature* **2017**, *546*, 632−636.

(16) Kortekaas, L.; Browne, W. R. The evolution of spiropyran: fundamentals and progress of an extraordinarily versatile photochrome. *Chem. Soc. Rev.* **2019**, *48*, 3406−3424.

(17) Han, B.; Zhang, Y.-L.; Zhu, L.; Li, Y.; Ma, Z.-C.; Liu, Y.-Q.; Zhang, X.-L.; Cao, X.-W.; Chen, Q.-D.; Qiu, C.-W.; Sun, H.-B. Plasmonic-Assisted Graphene Oxide Artificial Muscles. *Adv. Mater.* **2019**, *31*, No. 1806386.

(18) Cheng, X.; Sun, R.; Yin, L.; Chai, Z.; Shi, H.; Gao, M. Light-Triggered Assembly of Gold Nanoparticles for Photothermal Therapy and Photoacoustic Imaging of Tumors In Vivo. *Adv. Mater.* **2017**, *29*, No. 1604894.

(19) Pang, X.; Lv, J.-A.; Zhu, C.; Qin, L.; Yu, Y. Photodeformable Azobenzene-Containing Liquid Crystal Polymers and Soft Actuators. *Adv. Mater.* **2019**, *31*, No. 1904224.

(20) Bléger, D.; Hecht, S. Visible-Light-Activated Molecular Switches. *Angew. Chem., Int. Ed.* **2015**, *54*, 11338−11349.

(21) Camacho-Lopez, M.; Finkelmann, H.; Palffy-Muhoray, P.; Shelley, M. Fast liquid-crystal elastomer swims into the dark. *Nat. Mater.* **2004**, *3*, 307−310.

(22) Lu, W.; Le, X.; Zhang, J.; Huang, Y.; Chen, T. Supramolecular shape memory hydrogels: a new bridge between stimuli-responsive polymers and supramolecular chemistry. *Chem. Soc. Rev.* **2017**, *46*, 1284−1294.
(23) Ye, X.; Jin, L.; Caglayan, H.; Chen, J.; Xing, G.; Zheng, C.; Doan-Nguyen, V.; Kang, Y.; Engheta, N.; Kagan, C. R. Improved Size-Tunable Synthesis of Monodisperse Gold Nanorods through the Use of Aromatic Additives. *ACS Nano* **2012**, *6*, 2804−2817.
(24) Yun, J. H.; Li, C.; Chung, H.; Choi, J.; Cho, M. Multiscale modeling and its validation of the trans-cis-trans reorientation-based photodeformation in azobenzene-doped liquid crystal polymer. *Int. J. Solids Struct.* **2017**, *128*, 36−49.
(25) Nikoobakht, B.; El-Sayed, M. A. Preparation and Growth Mechanism of Gold Nanorods (NRs) Using Seed-Mediated Growth Method. *Chem. Mater.* **2003**, *15*, 1957−1962.
(26) Zhong, H.-Y.; Chen, L.; Yang, R.; Meng, Z.-Y.; Ding, X.-M.; Liu, X.-F.; Wang, Y.-Z. Azobenzene-containing liquid crystalline polyester with $\pi-\pi$ interactions: diverse thermo- and photo-responsive behaviours. *J. Mater. Chem. C* **2017**, *5*, 3306−3314.
(27) Zhang, H.; Fang, Y.; Yang, F.; Liu, X.; Lu, X. Aromatic organic molecular crystal with enhanced $\pi-\pi$ stacking interaction for ultrafast Zn-ion storage. *Energy Environ. Sci.* **2020**, *13*, 2515−2523.
(28) Ghosh, S. K.; Pal, T. Interparticle Coupling Effect on the Surface Plasmon Resonance of Gold Nanoparticles: From Theory to Applications. *Chem. Rev.* **2007**, *107*, 4797−4862.
(29) Pedrazzoli, D.; Manas-Zloczower, I. Understanding phase separation and morphology in thermoplastic polyurethanes nanocomposites. *Polymer* **2016**, *90*, 256−263.
(30) Huynh, T. P.; Sonar, P.; Haick, H. Advanced Materials for Use in Soft Self-Healing Devices. *Adv. Mater.* **2017**, *29*, No. 1604973.
(31) Zhu, S.; Hu, J. A Polyurethane Soft Actuator with Two Basic Contractions. *Mater. Today: Proc.* **2019**, *16*, 1456−1461.
(32) York, P. A.; Wood, R. J. In *A Geometrically-Amplified In-plane Piezoelectric Actuator for Mesoscale Robotic Systems*, 2017 IEEE International Conference on Robotics and Automation (ICRA), 2017; pp 1263−1268.
(33) Madden, J. D. W.; Vandesteeg, N. A.; Anquetil, P. A.; Madden, P. G. A.; Takshi, A.; Pytel, R. Z.; Lafontaine, S. R.; Wieringa, P. A.; Hunter, I. W. Artificial muscle technology: Physical principles and naval prospects. *IEEE J. Oceanic Eng.* **2004**, *29*, 706−728.
(34) Li, J.; Ma, W.; Song, L.; Niu, Z.; Cai, L.; Zeng, Q.; Zhang, X.; Dong, H.; Zhao, D.; Zhou, W.; Xie, S. Superfast-Response and Ultrahigh-Power-Density Electromechanical Actuators Based on Hierarchal Carbon Nanotube Electrodes and Chitosan. *Nano Lett.* **2011**, *11*, 4636−4641.
(35) Park, C. H.; Son, Y. S. In *Evaluation of Artificial Muscle Using SMA Spring Bundle with High Load Capacity and Power Density*, 2017 14th International Conference on Ubiquitous Robots and Ambient Intelligence, IEEE: New York, 2017; pp 81−82.
(36) Lima, M. D.; Li, N.; de Andrade, M. J.; Fang, S.; Oh, J.; Spinks, G. M.; Kozlov, M. E.; Haines, C. S.; Suh, D.; Foroughi, J.; Kim, S. J.; Chen, Y.; Ware, T.; Shin, M. K.; Machado, L. D.; Fonseca, A. F.; Madden, J. D. W.; Voit, W. E.; Galvao, D. S.; Baughman, R. H. Electrically, Chemically, and Photonically Powered Torsional and Tensile Actuation of Hybrid Carbon Nanotube Yarn Muscles. *Science* **2012**, *338*, 928−932.
(37) Haines, C. S.; Lima, M. D.; Li, N.; Spinks, G. M.; Foroughi, J.; Madden, J. D. W.; Kim, S. H.; Fang, S.; de Andrade, M. J.; Goktepe, F.; Goktepe, O.; Mirvakili, S. M.; Naficy, S.; Lepro, X.; Oh, J.; Kozlov, M. E.; Kim, S. J.; Xu, X.; Swedlove, B. J.; Wallace, G. G.; Baughman, R. H. Artificial Muscles from Fishing Line and Sewing Thread. *Science* **2014**, *343*, 868−872.
(38) Inoue, H.; Yoshiyama, T.; Hada, M.; Chujo, D.; Saito, Y.; Nishikawa, T.; Yamashita, Y.; Takarada, W.; Matsumoto, H.; Hayashi, Y. High-performance structure of a coil-shaped soft-actuator consisting of polymer threads and carbon nanotube yarns. *AIP Adv.* **2018**, *8*, No. 075316.
(39) Niino, T.; Egawa, S.; Kimura, H.; Higuchi, T. In *Electrostatic Artificial Muscle: Compact, High-Power Linear Actuators with Multiple-Layer Structures*, Proceedings IEEE Micro Electro Mechanical Systems. An Investigation of Micro Structures, Sensors, Actuators, Machines and Robotic Systems (Cat. No.94CH3404-1), 1994; pp 130−135.
(40) Oh, J.; Kozlov, M. E.; Carretero-González, J.; Castillo-Martínez, E.; Baughman, R. H. Thermal actuation of graphene oxide nanoribbon mats. *Chem. Phys. Lett.* **2011**, *505*, 31−36.
(41) Mu, J.; Hou, C.; Zhu, B.; Wang, H.; Li, Y.; Zhang, Q. A multi-responsive water-driven actuator with instant and powerful performance for versatile applications. *Sci. Rep.* **2015**, *5*, No. 9503.
(42) Ma, M.; Guo, L.; Anderson, D. G.; Langer, R. Bio-Inspired Polymer Composite Actuator and Generator Driven by Water Gradients. *Science* **2013**, *339*, 186−189.
(43) Zhang, J.; Sheng, J.; O'Neill, C. T.; Walsh, C. J.; Wood, R. J.; Ryu, J.-H.; Desai, J. P.; Yip, M. C. Robotic Artificial Muscles: Current Progress and Future Perspectives. *IEEE Trans. Rob.* **2019**, *35*, 761−781.
(44) Link, S.; El-Sayed, M. A. Spectral Properties and Relaxation Dynamics of Surface Plasmon Electronic Oscillations in Gold and Silver Nanodots and Nanorods. *J. Phys. Chem. B* **1999**, *103*, 8410−8426.
(45) Yu, Q.; Yang, X. J.; Chen, Y.; Yu, K. Q.; Gao, J.; Liu, Z. F.; Cheng, P.; Zhang, Z. J.; Aguila, B.; Ma, S. Q. Fabrication of Light-Triggered Soft Artificial Muscles via a Mixed-Matrix Membrane Strategy. *Angew. Chem., Int. Ed.* **2018**, *57*, 10192−10196.
(46) Bisoyi, H. K.; Li, Q. Light -Driven Liquid Crystalline Materials: From Photo -Induced Phase Transitions and Property Modulations to Applications. *Chem. Rev.* **2016**, *116*, 15089−15166.
(47) Choi, J.; Chung, H.; Yun, J.-H.; Cho, M. Photo-isomerization effect of the azobenzene chain on the opto-mechanical behavior of nematic polymer: A molecular dynamics study. *Appl. Phys. Lett.* **2014**, *105*, No. 221906.
(48) Moon, J.; Choi, J.; Cho, M. Opto-mechanical behavior and interfacial characteristics of crosslinked liquid crystalline polymer composites with carbon nanotube fillers. *Carbon* **2017**, *121*, 181−192.
(49) Chung, H.; Choi, J.; Yun, J. H.; Cho, M. Nonlinear photomechanics of nematic networks: upscaling microscopic behaviour to macroscopic deformation. *Sci. Rep.* **2016**, *6*, No. 20026.
(50) Li, M.; Lv, S.; Zhou, J. Photo-thermo-mechanically actuated bending and snapping kinetics of liquid crystal elastomer cantilever. *Smart Mater. Struct.* **2014**, *23*, No. 125012.

https://dx.doi.org/10.1021/acs.chemmater.0c04170
Chem. Mater. 2021, 33, 987−997